JOURNAL OF AIRCRAFT
Vol. 40, No. 4, July–August 2003

Experimental Analysis and Modeling of Limit Cycles in a Dynamic Wind-Tunnel Rig

Paul M. Davison,* Mark H. Lowenberg,† and Mario di Bernardo‡
University of Bristol, Bristol, England BS8 1TR, United Kingdom

Large-amplitude self-sustaining periodic oscillations have been observed in an unforced pitch-axis single-degree-of-freedom dynamic wind-tunnel rig. These limit-cycle oscillations and the associated bifurcations are caused by aerodynamic phenomena and have been studied by constructing experimental bifurcation diagrams, where a system parameter (horizontal tailplane deflection) is varied quasi statically and the steady-state response of the system recorded. An innovative strategy based on these bifurcation diagrams is then used to identify a mathematical model of the rig aerodynamics over a wide operating region. Good agreement is shown between numerical simulations of the theoretical model and experimental time histories over a large range of angle-of-attack and tailplane deflections.

Nomenclature

A = limit-cycle amplitude
A_u = parameter of the tanh function (Fig. 7)
B = exponential growth or decay rate
C_m = aircraft pitching moment coefficient
$\bar{c}$ = aircraft mean aerodynamic chord
I = aircraft pitch moment of inertia
K = growth/decay rate of tanh function
N = number of subintervals
S = aircraft wing surface area
T = time interval
t = time
V = aircraft velocity (tunnel velocity)
Δ = parameter of the tanh function (Fig. 7), $\frac{1}{2}(A_u - A)$
δ_e = symmetrical horizontal tailplane deflection
θ = aircraft pitch angle to horizontal (angle-of-attack)
$\hat{\theta}$ = estimated pitch angle to horizontal
θ = aircraft pitch rate, q and $\mathrm{d}\theta/\mathrm{d}t$
$\dot{\hat{\theta}}$ = estimated model pitch rate, $\hat{q}$
ρ = air density
ϕ = phase angle
ω = limit-cycle frequency

I. Introduction

TO gain a tactical advantage in close-combat aerial scenarios, it is desirable to have superior maneuverability.[1] Increased maneuverability requires high rates of change of motion variables, which, when occurring at large angles of attack and sideslip, produce strong coupling between aerodynamics, inertial terms, and control surface deflections and a strong dependence on frequency and amplitudes of motions. This coupling is, as yet, impossible to predict using analytical or computational means in all but the simplest cases; hence, some form of subscale testing is required.

Dynamic wind-tunnel test rigs can take many forms.[2,3] Most are of the direct forced type, which produce constant rotation or sinusoidal oscillations about a single axis. To allow large models to be tested, the support structures and drive systems are usually large, which increases the cost of performing such tests. Moreover, because the oscillations/rotations are usually about a single axis at a time, it may be necessary to use several different rigs to obtain a full set of dynamic derivatives.[4]

Ongoing work at the University of Bristol to develop a multi-axis unforced wind-tunnel rig, the pendulum support rig,[5] is underway to address some of the problems associated with obtaining dynamic derivatives, most notably complexity and cost. The rig is multipurpose in nature; it can be used for aerodynamic modeling (where periodic and arbitrary motions can be generated) and control system design and evaluation using active control surfaces. It is envisaged that the rig will allow integration of the aerodynamic modeling and control system design cycles, during the aircraft development phase, into a single parallel process.

In this paper an experimental investigation is presented of the nonlinear behavior of the rig in a single degree of freedom (DOF). (For more information on general nonlinear dynamics, see, for example, Ref. 6, or on experimental nonlinear dynamics, see Ref. 7.) The current model [British Aerospace, Ltd. (BAe) Hawk] produces some interesting nonlinear behavior in the form of self-sustained, periodic oscillations (limit-cycle oscillations). Experimental bifurcation diagrams are presented and are shown to provide a quick and simple tool for examining the global dynamics of the system. (Experimental bifurcation diagrams were also used in Ref. 8 to analyze flutter.) No attempt is made to identify the flow phenomenon causing the behavior. However, with the use of experimental bifurcation analysis, a mathematical model is derived that captures the dynamics of the rig. Modeling using traditional stability derivative methods will allow limit cycles to be represented, as long as the derivatives are nonlinear functions of states and parameters; however, the derivatives would have to be extracted and stored in look-up tables. A more efficient solution, particularly where the aerodynamics is highly nonlinear and includes bifurcation phenomena, is to develop a model in which observed parameters such as limit-cycle amplitude, stability, and frequency can be specified explicitly in the model. We show how this information can be embedded into an appropriate dynamic estimator of the experimental system by using the results of the experimental bifurcation analysis.

The rest of the paper is arranged as follows. In Sec. II previous aerodynamic modeling approaches that have been used to capture limit-cycle oscillations are outlined. In Sec. III, the experimental apparatus is described in more detail. In Sec. IV, the behavior of the rig is described, and experimental bifurcation diagrams, time histories, and phase-plane plots are presented. In Sec. V, the novel modeling method is described in detail, before validation of the model is presented in Sec. VI, and generalization issues are discussed.

Received 30 September 2002; revision received 8 October 2002; accepted for publication 3 April 2003.

*Postgraduate Student, Departments of Aerospace Engineering and Engineering Mathematics, Faculty of Engineering, Queen's Building, University Walk. Student Member AIAA.

†Lecturer in Flight Dynamics, Department of Aerospace Engineering, Faculty of Engineering, Queen's Building, University Walk. Senior Member AIAA.

‡Lecturer in Non-Linear Systems, Department of Engineering Mathematics, Faculty of Engineering, Queen's Building, University Walk.

II. Aerodynamic Modeling Issues

Aerodynamic modeling for the purposes of flight dynamics involves representing the aerodynamic loads in a formulation suitable for use in the equations of motion for arbitrary flight conditions. Typically, the forces and moments are functions of the motion variables and parameters, such as control inputs, undercarriage position, etc. The vast majority of such models are quasi steady and capture only small-amplitude motions. Where limit-cycle motions are known to exist, quasi-steady derivative type models can capture aspects of their dynamics. The usual limit-cycle phenomenon is wing rock: a lateral–directional oscillation, dominant in roll, that occurs in many fighter aircraft configurations as angle of attack is increased.[9,10] Its onset corresponds to loss in stability of the Dutch roll mode, which can be reflected in the stability derivatives relatively easily. The bounded oscillation is achieved by adopting a nonlinear dependence of roll damping coefficient on the state. Whereas the steady-state characteristics can be adequately represented in this manner, it is very difficult to model the transient behavior, stability of the orbits, and bifurcationary events following the growth of the cycle.

It has been recognized that unsteady effects can become significant in rapid maneuvers, or maneuvers at very low forward speeds. Quasi-steady derivative-type models are inadequate in accounting for time-dependent aerodynamic reactions. A substantial body of work has, therefore, been undertaken on advanced modeling techniques to capture these effects, for example, Ref. 5. 11–14. However, practical implementation of such methods has not as yet been extended to bifurcation and large-amplitude phenomena such as limit cycles.

The majority of limit-cycle modeling work has been in connection with wing rock. Relatively few aircraft exhibit longitudinal pitching limit-cycle oscillations (bucking) as in the case of the pendulum rig Hawk model at Bristol. (In fact, if the Hawk model is mounted with lateral–directional DOF as well as longitudinal, the bucking behavior is likely to be preceded by a lateral–directional phenomenon, such as wing rock or departure to incipient spin.)

Most of the aerodynamic models derived to represent wing rock from experimental data are single-DOF, although 3-DOF coupled lateral–directional motions have also been explored.[10,15] In all cases, some form of nonlinear roll damping has been incorporated into the formulation and efforts have been made to correlate amplitude and sometimes frequency with measured data, for example, Refs. 15–18; the amplitude of the limit cycle depends on the ratio of linear to nonlinear damping terms. Model structures with discontinuities and/or hysteresis in aerodynamic derivatives have also been used to represent wing rock motions.[19–21] Wing rock limit cycles can also be obtained from relatively simple models in which kinematic coupling between longitudinal and lateral–directional modes occurs.[20,22] A longitudinal bucking-type limit cycle has been modeled in Ref. 22 but this uses a jump in lift coefficient associated with stall, which is not appropriate to the Hawk case.

Both wing rock and aerofoil pitching oscillations have been analyzed in the context of bifurcation theory in Ref. 23. Models incorporating nonlinear damping were evaluated in terms of bifurcation behavior leading to limit cycles; the nature of the bifurcations (sub- or supercritical) was assessed, as was the rate of growth of the periodic orbits. However, the identification of model structures suitable for representing global bifurcation behavior over a wide operating envelope, as observed with the Hawk model (see Sec. IV), has not been addressed elsewhere.

As with all flight dynamics modeling, a balance must be struck between fine detail in localized regions and the need to represent behavior over a very large operating envelope. Bifurcation analysis can be an invaluable tool in understanding the structure and dynamic features of a flight dynamics model. When tools to analyze and characterize different dynamic transitions are provided, it can help to identify the main features to be captured by the model. Therefore, in this paper, the bifurcation behavior and limit-cycle features are modeled in an approximate manner, with parameters and states as independent variables. The method makes assumptions about the shape of the periodic orbits and about the location and nature of unstable stationary points but is able to capture most of the bifurcation behavior exhibited in rigid-body flight mechanics to within a degree of accuracy sufficient for flight mechanics analysis. It uses explicitly the results of the bifurcation analysis performed on the experimental rig.

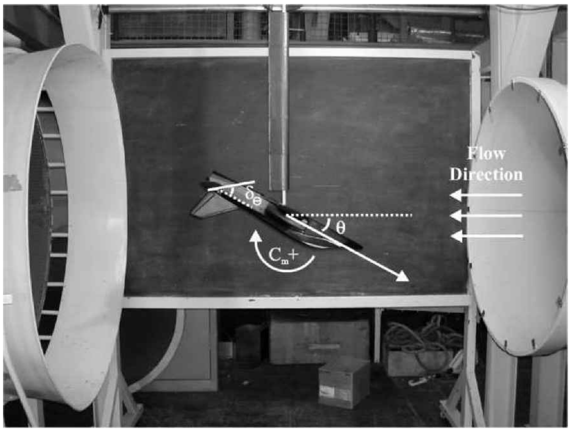

Fig. 1 Hawk model mounted inverted in the department open-jet tunnel.

III. Experimental Rig

For the tests presented in this paper, the rig was mounted inverted in the 1.1-m-diam open-jet tunnel at the University of Bristol (Fig. 1). The tunnel has a maximum speed of 40 m/s, with a turbulence level of approximately 2% at 20 m/s at the time of these tests. (Minor modifications have since been made to the tunnel, resulting in lower turbulence levels.) All tests were performed at 20 m/s (corresponding to $Re = 0.2 \times 10^6$ based on wing chord of the model).

An approximate 1/16th-scale BAe Hawk model was used for the tests, constructed mainly of fiberglass covered wood. The weight of the model without gimbal is 1.8 kg, and the main dimensions are wing span 0.612 m, length 0.655 m, wing surface area 0.078 m^2, and mean aerodynamic chord 0.135 m. For the results reported here, the model was free to rotate in a single-DOF (pitch) on a custom-made aluminium gimbal, using precision ball bearings to minimize friction. Moment of inertia in pitch is 0.0343 $kg \cdot m^2$ when balanced about the pivot point, measured using the trifilar suspension technique.[24] Model pitch angle was sensed using a high-accuracy carbon film potentiometer (accurate to ± 0.05 deg) and a solid-state rate gyro (± 0.25 deg/s accuracy) was mounted in the model to give direct pitch rate measurements. The all-moving tailplanes were directly driven by miniature model aircraft servos using pulse-width modulation (PWM). Control and data acquisition were performed using a dSPACE DS1103 real-time control system. This consists of an internal personal computer card with two digital signal processors and an external break-out box. The system has 16, 16-bit analog-to-digital converters, which are used for acquisition of pitch angle and pitch rate, and several PWM outputs used to drive the active control surfaces. No filtering was applied to the data, and all sampling was performed at 100 Hz.

IV. Experimental Results

Typically, as tailplane angle δ_e is decreased the angle of attack α of the aircraft will increase, leading to a negative overall slope on the δ_e–α bifurcation diagram. In general, aerodynamic nonlinearities will cause a reduction in stability at higher α, which can lead to loss of control, even with large control surface deflections. This loss of stability can be longitudinal (in the form of deep stall or pitch oscillations), but usually occurs in the lateral–directional sense, for example, see Ref. 25. It is possible, particularly in delta-wing aircraft and those with long forebodies, for a Hopf bifurcation to a stable limit cycle to occur, mainly in the roll sense, at high α before there is a total loss of stability. As already mentioned, this phenomenon is known as wing rock, for example, see Refs. 9 and 10.

Another nonlinear phenomenon that occurs at high α is the fold bifurcation. This is characterized by a branch of stable equilibria (stationary points) folding back on itself and becoming unstable. This bifurcation is associated with jump-type behavior where, under parameter variations, stability is lost suddenly, often ending in deep stall or departure into a spin.

With the present rig, there are no lateral–directional modes present. Static tests have shown the model to be statically stable over the range $-10 < \alpha < 35$ deg, $-50 < \delta_e < 10$ deg. However, spring-oscillation tests in the department 7×5 ft closed-section tunnel have shown regions of low pitch damping at approximately $\alpha \approx 5$ and $\alpha \approx 15$ deg (Ref. 5). The existence of large-amplitude nonlinear pitching behavior was not known before free-motion testing.

Three types of experiments were performed to 1) investigate the system bifurcation behavior, 2) record time trajectories, and 3) deduce the stability of a desired equilibrium solution. Testing specifics follow.

1) To construct experimental bifurcation diagrams, it was necessary to perform tests where the horizontal tailplane deflection was varied slowly enough for the system behavior not to be affected by transients. Typically, for the rig under investigation, this required sweeping the tailplane deflection from one position limit to the other over 1 h. These tests establish the stable attractors of the system with respect to a parameter (in this case, tailplane deflection δ_e). They also show any bifurcation phenomena present in the rig, that is, qualitative changes in the system long-term behavior as the tailplane angle is varied.

2) To collect data for phase-plane plots and time histories, tests were performed where the horizontal tailplane deflection remained constant while the corresponding time histories of the rig evolution were recorded.

3) To deduce the stability of a given solution at discrete tailplane deflections, tests were performed where, again, the horizontal tailplane remained in a constant position but the model was held at a large positive or negative pitch angle before being released and time histories recorded.

Figure 2 shows the results of two experimental bifurcation runs: 1) for decreasing (Fig. 2a) and 2) for increasing (Fig. 2b) tailplane deflection. Each run lasted 60 min. To plot the experimental bifurcation diagrams (or more precisely, orbit diagrams,[6] a form of bifurcation diagram where only attractors are plotted), nonstationary points (points where pitch rate q was nonzero) were discarded. This gives a diagram of fixed points and maximum limit-cycle amplitudes for the system as a function of tailplane deflection. Because of experimental noise and tunnel turbulence, it was not possible to plot only those points at which pitch rate was zero; therefore a tolerance band of $|q| < 2$ deg/s was applied.

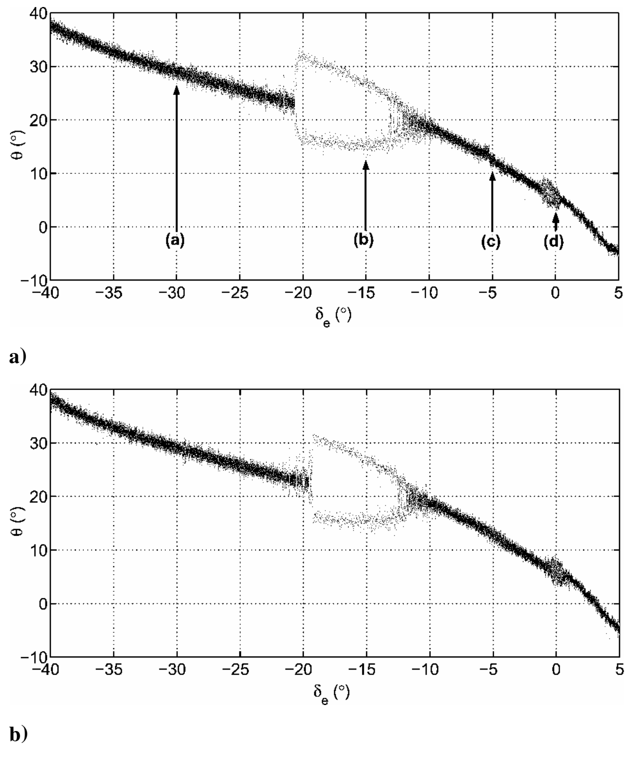

Fig. 2 **Experimental bifurcation diagrams: a) for decreasing tailplane deflection and b) for increasing tailplane deflection.**

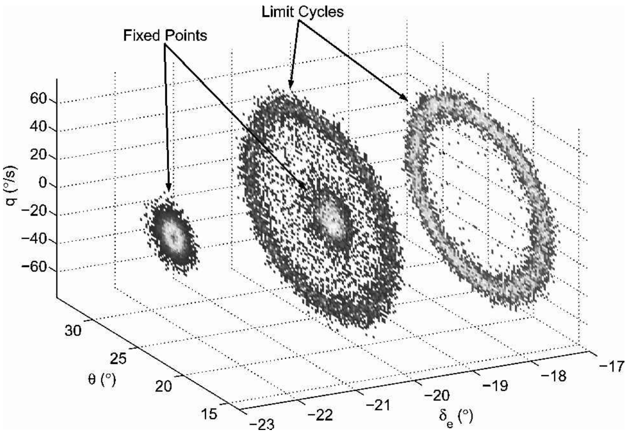

Fig. 3 Phase plane plots for three fixed tailplane deflections, $\delta_{e1} = -17.5$, $\delta_{e2} = -20.0$, and $\delta_{e3} = -22.5$ deg, where lighter regions show more time spent at that phase-plane point.

The behavior seen in Fig. 1a at approximately $\delta_e \approx -12$ deg can be characterized as a supercritical Hopf bifurcation to a limit cycle. This is indicated by the slow growth of the limit cycle from the branch of equilibria as tailplane angle is reduced, that is, the fixed-point solution branch becomes unstable and the system follows the stable limit-cycle branch. Oscillation amplitude increases with decreasing tailplane angle until at approximately $\delta_e \approx -21$ deg the system exhibits a sudden jump back to a stable fixed point (Fig. 1a). This stable branch continues to the maximum elevator deflection.

With increasing tailplane angle (Fig. 1b), the jump from stable fixed point to limit cycle occurs at approximately $\delta_e \approx -19{\cdot}5$ deg. This hysteresis and jump behavior indicates the presence of a subcritical Hopf point at $\delta_e \approx -19{\cdot}5$ deg. This is where, as tailplane deflection is increased, the stable fixed-point branch becomes unstable and the system jumps to the nearest attractor, the limit cycle.

Further evidence of this phenomenon is given in Fig. 3, which shows three phase plane plots taken at fixed tailplane deflections. For each tailplane setting, data were recorded for 15 min. It can be seen that at $\delta_e \approx -17{\cdot}5$ deg there is a well-established stable limit cycle denoted by the circle in the θ–$\dot{\theta}$ plane. At $\delta_e \approx -22{\cdot}5$ deg, there is a stable fixed point (a point in the θ–$\dot{\theta}$ plane, enlarged by noise and turbulence), and at $\delta_e \approx -20$ deg, a stable limit cycle and stable fixed point coexist and are characterized by different basins of attraction. These attractors correspond to those seen in the experimental bifurcation diagrams (Fig. 1). Unfortunately, because of relatively large amounts of turbulence in the wind tunnel, it is not possible to release the model from different starting points and find the basins of attraction of the equilibria in the hysteresis region. While recording data for the phase plane plot with $\delta_e \approx -20$ deg in Fig. 3, occasionally the tunnel turbulence would be great enough to force the model away from its present steady state, past an unstable branch (which cannot be found experimentally), and onto the other coexisting steady state. The resulting transients correspond to the many points that lie between the limit cycle and the fixed point in Fig. 3.

Figures 4a–4d show time histories corresponding to the fixed tailplane deflections labeled in Fig. 1a Note the effect of low-frequency tunnel turbulence on the system trajectories. As expected, points a and c are fixed equilibria at approximately $\theta \approx 28$ and $\theta \approx 12$ deg, respectively. Point b in Fig. 1 is instead a large-amplitude limit-cycle oscillation, centered at $\theta \approx 22$ deg with an amplitude of approximately 10 deg. This is confirmed by the experimental time

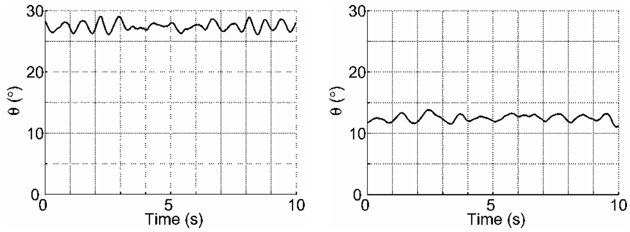

a) $\delta_e = -30$ deg c) $\delta_e = -5$ deg

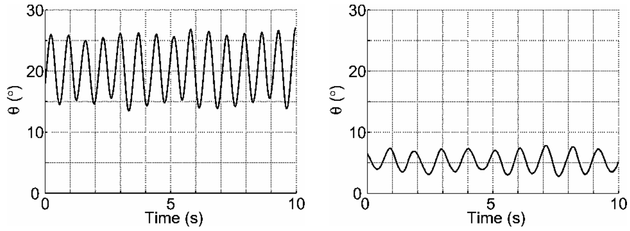

b) $\delta_e = -15$ deg d) $\delta_e = 0$ deg

Fig. 4 Time histories for points a–d in Fig. 1a.

history shown in Fig. 4b. The experimental bifurcation diagram also reveals a region of small-amplitude limit cycles at point d, centered at approximately $\theta = 5$ deg. This corresponds well with a region of low pitch damping identified in small-amplitude spring oscillation tests.[5]

Note that tunnel turbulence can become a problem when distinguishing fixed points from small-amplitude limit cycles, for example, smaller than the tolerance band considered. This is particularly relevant for determining the exact location of the Hopf bifurcation points. Close to these points, limit cycles have small amplitudes, and therefore, other indicators such as periodicity need to be used to locate them with greater accuracy.

It is thought that the large-amplitude limit cycle exhibited by the model is caused by a reduction in pitch damping caused by the tailplanes becoming immersed in the wake of the wing at angles of attack from approximately 18 to 23 deg. Whereas this is a specific phenomenon occurring with this model configuration, it is an interesting experimental example of an application of nonlinear dynamics theory that has relevance in the analysis of full-scale aircraft dynamics.

V. Model Formulation

Unlike systems that show no bifurcation or nonlinear behavior, the main requirement in this case is for the model to capture the predominant features of the bifurcations and oscillatory behavior exhibited by the experimental rig. Therefore, the challenge is to find a single model structure that can represent the whole system and estimate correctly the dynamics observed experimentally.

In particular, we require that the bifurcation diagram of the model exhibits the main features of the experimental bifurcation diagram shown in Fig. 1. These are are summarized in Fig. 5, where the type of asymptotic solution present at each tailplane deflection and the location of the relevant bifurcation points are shown.

As a starting point, we examine a typical experimental time history of the rig position, such as the one shown in Fig. 6, where the tailplane deflection is fixed at −15 deg and the rig is released from a phase-space point away from the limit cycle.

Notice from Fig. 6, that the oscillations appear approximately sinusoidal with an exponential-type decay. Also visible are the effects of turbulence on the system (especially at $t \approx 10$ s). When it is assumed that the oscillations are symmetrical about the fixed point and the effects of turbulence are neglected, this suggests that the position decays onto the stable period-1 limit cycle according to (as in Ref. 26)

$$\theta = A(1 + e^{-Bt})\sin(\omega t + \phi) \tag{1}$$

Using an exponential function to model the decreasing envelope was found to give problems due to the divergence of the exponential for $t \to -\infty$ (Fig. 7a). In fact, this makes it difficult to account for transitions from a stable limit cycle to an equilibrium or a smaller amplitude cycle, such as those actually observed experimentally, for example, in the hysteretic region.

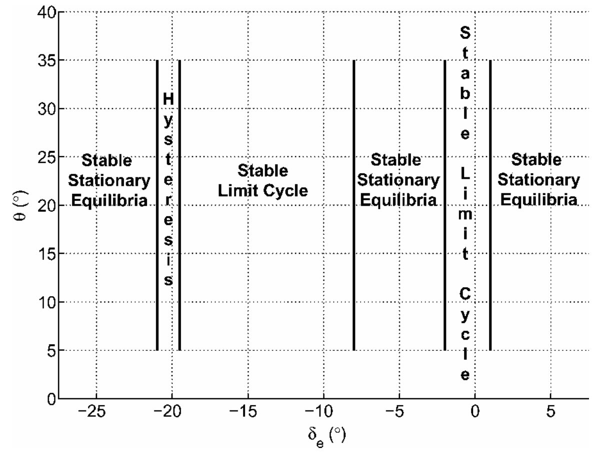

Fig. 5 Schematic of the main features of the desired model bifurcation diagram, that is, attractor types and bifurcation points.

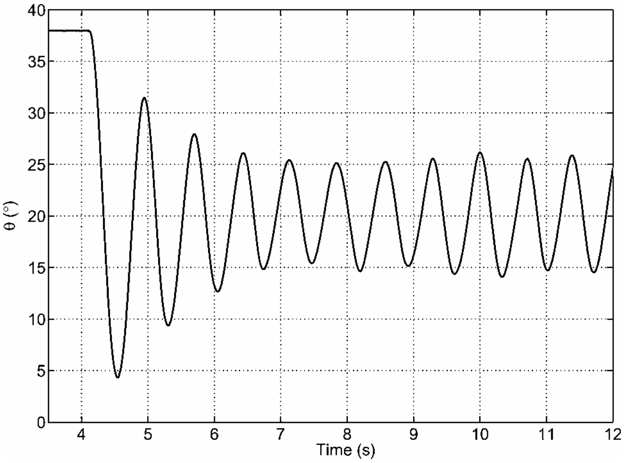

Fig. 6 Experimental time history showing decay onto the limit cycle; (δ_e fixed at −15 deg.

To overcome this problem, a tanh function was selected to model the envelope because this gives the required growth/decay shape (Fig. 7b). Thus, we choose

$$\theta = \{A_u - \Delta[1 + \tanh(Kt)]\}\sin(\omega t + \phi) \tag{2}$$

where A_u and Δ are extra parameters necessary for defining the tanh function characteristics and K [equivalent to B in Eq. (1)] defines the growth/decay rate. Note that the parameter A_u in Eq. (2) can be made arbitrarily large if necessary to model pure exponential growth/decay from/to $\pm\infty$. (A_u has an interesting interpretation, when modeling the evolution of the system from a given limit cycle to another attractor. In this case, A_u corresponds to the amplitude of the limit cycle from which the evolution begins.)

Differentiating Eq. (2) with respect to time, we can now get an estimate for the pitch rate $\dot{\theta}$ as

$$\begin{aligned}\dot{\theta} &= \{A_u - \Delta[1 + \tanh(Kt)]\}\omega\cos(\omega t + \phi)\\ &\quad - K\Delta\mathrm{sech}^2(Kt)\sin(\omega t + \phi)\end{aligned} \tag{3}$$

and by further differentiation the acceleration,

$$\begin{aligned}\ddot{\theta} &= -\omega^2\theta - 2K\Delta\omega\cos(\omega t + \phi)\mathrm{sech}^2(Kt)\\ &\quad + 2K^2\Delta\sin(\omega t + \phi)\mathrm{sech}^2(Kt)\tanh(Kt)\end{aligned} \tag{4}$$

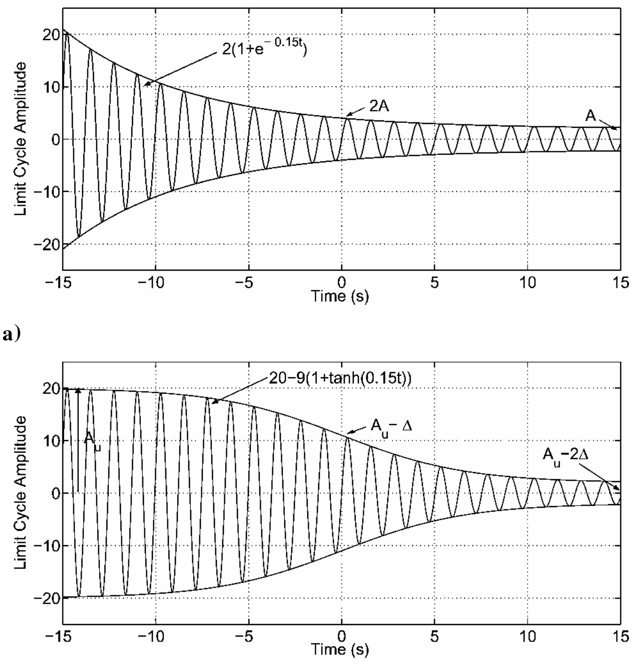

a)

b)

Fig. 7 Time histories for a) exponential and b) tanh function decay to a limit cycle.

Our aim, now, is to use Eqs. (2–4) to construct a suitable dynamic estimator of the experimental rig. Namely, given a certain initial position θ_0 and pitch rate $\dot{\theta}_0$, we want the model to provide an estimate of the system trajectory over a desired time range. In so doing, we need to address two separate problems: 1) establishing an appropriate methodology to carry out the estimation and 2) evaluating all of the necessary parameters involved in the estimation process. We start by addressing the former problem, leaving to Sec. V.B the solution of the latter.

A. Estimation Strategy

The first, more immediate solution to carry out the estimation could be to integrate Eq. (4) directly with initial conditions θ_0 and $\dot{\theta}_0$. Although it provides an acceptable estimate under nominal operating conditions, this methodology would fail to reproduce transient behavior due to sudden disturbances, parameter variations, or noise. This is because Eq. (4) is derived on the assumption that the position envelope is monotonically decreasing (or increasing). Thus, the effect of any disturbance occurring when the envelope has already become too small would be artificially attenuated by the model (example in Sec. V.2A). To overcome this problem, one would need to reset the integration time whenever an undesired event or parameter variation occurs. This is difficult or even impossible to implement on-line because it would require some robust event-driven integration algorithm relying on an efficient event-detection routine.

Therefore, we consider an alternative strategy that uses a combination of Eqs. (2–4) and time discretization. Namely, suppose we want to simulate the system trajectory from θ_0 and $\dot{\theta}_0$ over a given time interval, for example, $T = (t_{\max} - t_{\min})$. Let $\delta t = (t_{\max} - t_{\min})/N$ be a discretization of T into N sufficiently small subintervals. Then, the key idea is to exploit knowledge of the position and pitch rate, θ_n and $\dot{\theta}_n$, at the generic nth step, to derive an estimate of the corresponding acceleration $\ddot{\theta}_n$ and use this to find estimates of the position and pitch rate, θ_{n+1} and $\dot{\theta}_{n+1}$ at the next step, $n+1$. More precisely, from Eqs. (2) and (3) we know that

$$\theta = f(t, \phi, \boldsymbol{\mu}) \tag{5}$$

$$\dot{\theta} = g(t, \phi, \boldsymbol{\mu}) \tag{6}$$

where f and g are the left-hand sides of Eqs. (2) and (3) and $\boldsymbol{\mu}$ is the vector of parameters. Hence, considering the time t as an independent variable, which for the sake of clarity we relabel as τ, we then have at the nth step that

$$\theta_n - f(\tau_n, \phi_n, \boldsymbol{\mu}) = 0 \tag{7}$$

$$\dot{\theta}_n - g(\tau_n, \phi_n, \boldsymbol{\mu}) = 0 \tag{8}$$

In other words, we know that, for any given value of position θ_n and pitch rate $\dot{\theta}_n$, if the parameters $\boldsymbol{\mu}$ are fixed, there exist a τ_n and ϕ_n that solve Eqs. (7) and (8). Thus, Eqs. (7) and (8) define implicitly τ_n and ϕ_n as functions of the position and pitch rate at each step, that is,

$$\tau_n = \zeta(\theta_n, \dot{\theta}_n, \boldsymbol{\mu}) \tag{9}$$

$$\phi_n = \eta(\theta_n, \dot{\theta}_n, \boldsymbol{\mu}) \tag{10}$$

Hence, it is theoretically possible to use Eqs. (9) and (10) to find values for τ_n and ϕ_n given the current pitch angle θ and pitch rate $\dot{\theta}$. These values can then be substituted into Eq. (4) to find an estimate of the pitch acceleration (and pitching moment, if required) at the same step, that is,

$$\ddot{\theta}_n = \sigma(\tau_n, \phi_n, \boldsymbol{\mu}) \tag{11}$$

Finally, the position and pitch rate at the next step can be estimated (if δt is sufficiently small) as

$$\theta_{n+1}(t) = \theta_n + \ddot{\theta}_n(\delta t)^2 \tag{12}$$

$$\dot{\theta}_{n+1}(t) = \dot{\theta}_n + \ddot{\theta}_n \delta t \tag{13}$$

The fundamental open problem for this approach to work is to be able to derive τ_n and ϕ_n from Eqs. (2) and (3), given specific values of the position and pitch rate. In general, these are transcendental equations, which cannot be solved explicitly. In what follows we will see that τ_n and ϕ_n can indeed be found at each step by appropriate algebraic manipulations.

1. *Finding τ_n and ϕ_n*

Assume that the position θ_n and pitch rate $\dot{\theta}_n$ are given. Let

$$\Psi(\tau_n) = A_u - \Delta[1 + \tanh(K\tau_n)] \tag{14}$$

From Eq. (2), we then get

$$\phi_n = \arcsin[\theta_n/\Psi(\tau_n)] - \omega\tau_n \tag{15}$$

Substituting Eq. (15) into Eq. (3) gives

$$\begin{aligned}\dot{\theta}_n = {} & \Psi(\tau_n)\omega\cos\{\arcsin[\theta_n/\Psi(\tau_n)]\} \\ & - K\Delta\operatorname{sech}^2(K\tau_n)\sin\{\arcsin[\theta_n/\Psi(\tau_n)]\}\end{aligned} \tag{16}$$

Since

$$\cos[\arcsin(x)] \equiv \sqrt{1 - x^2} \tag{17}$$

we then have

$$\dot{\theta}_n = \Psi(\tau_n)\omega\sqrt{1 - \left[\frac{\theta_n}{\Psi(\tau_n)}\right]^2} - \frac{K\Delta\theta_n\operatorname{sech}^2(K\tau_n)}{\Psi(\tau_n)} \tag{18}$$

Rearranging Eqs. (18), we obtain

$$\dot{\theta}_n\Psi(\tau_n) + K\Delta\theta_n\operatorname{sech}^2(K\tau_n) = \Psi(\tau_n)^2\omega\sqrt{1 - [\theta_n/\Psi(\tau_n)]^2} \tag{19}$$

thus,

$$\begin{aligned}\Rightarrow \dot{\theta}_n^2\Psi(\tau_n)^2 + 2K\Delta\theta_n\dot{\theta}_n\Psi(\tau_n)\operatorname{sech}^2(K\tau_n) + K^2\Delta^2\theta_n^2\operatorname{sech}^4(K\tau_n) \\ = \omega^2\Psi(\tau_n)^4 - \omega^2\theta_n^2\Psi(\tau_n)^2\end{aligned} \tag{20}$$

Now, from Eq. (14),

$$\operatorname{sech}^2(K\tau_n) = 1 - \tanh^2(K\tau_n) = -\Psi(\tau_n)^2/\Delta^2 + 2\Psi(\tau_n)A_u/\Delta^2 - 2\Psi(\tau_n)/\Delta - A_u^2/\Delta^2 + 2A_u\Delta \tag{21}$$

Substituting Eq. (21) into Eq. (20) gives a quartic in $\Psi(t)$,

$$\begin{aligned}\Psi(\tau_n)^4(-\omega^2 + R/\Delta^4) &+ \Psi(\tau_n)^3[-S/\Delta^2 + R(4/\Delta^3 - 4A_u/\Delta^4)]\\ &+ \Psi(\tau_n)^2[\dot{\theta}_n^2 + \omega^2\theta^2 + S(2A_u/\Delta^2 - 2/\Delta)\\ &+ R(6A_u^2/\Delta^4 - 12A_u/\Delta^3 + 4/\Delta^2)]\\ &+ \Psi(\tau_n)[S(2A_u/\Delta - A_u^2/\Delta^2)\\ &+ R(12A_u^2/\Delta^3 - 4A_u^3/\Delta^4 - 8A_u/\Delta^2)]\\ &+ R(4A_u^2/\Delta^2 + A_u^4/\Delta^4 - 4A_u^3/\Delta^3) = 0\end{aligned} \tag{22}$$

where

$$R = K^2\Delta^2\theta_n^2 \tag{23}$$

$$S = 2K\Delta\theta_n\dot{\theta}_n \tag{24}$$

The roots of this quartic, $\Psi(\tau_n) = \Psi$, can then be used to find a value for τ_n. From Eq. (14), we get

$$\tau_n = (1/K)\operatorname{arctanh}[(A_u - \Psi)/\Delta - 1] \tag{25}$$

Note that, because Eq. (22) admits multiple solutions, we need to choose the one that when substituted in Eq. (25) gives an admissible real-valued τ_n. This is limited by the domain of the arctanh function, which lies between -1 and 1. Hence, we choose a positive real root from Eq. (22).

Substituting τ_n into Eq. (4), we then get an estimate of $\ddot{\theta}_n$, that is, the pitch acceleration at the nth step, that can be used in Eqs. (12) and (13) to find an estimate of θ_{n+1} and $\dot{\theta}_{n+1}$. Note that the pitch DOF equation of motion can then be used to solve for the pitching moment coefficient C_m given by

$$C_m = \frac{I\ddot{\theta}}{\frac{1}{2}\rho V^2 Se} \tag{26}$$

2. Examples

For the sake of clarity, we now use a representative example to illustrate the estimation strategy described. We assume that all of the necessary parameters have been found using the strategy that will be presented in Sec. V.B. A more extensive validation of the rig model will be presented in Sec. VI.

We consider a model of the experimental system with fixed tailplane deflection $\delta_e = -20$ deg. The experimental bifurcation diagram in Fig. 1 shows that, at this value of the tailplane deflection, there is a stable fixed point at $\theta = 23$ deg and a stable limit cycle of amplitude 6 deg. Time histories produced by the described estimation strategy for different starting points are shown in Fig. 8. Figure 9a shows the pitch reaction surface[27] produced by using Eq. (26). It is difficult to see the structure of the surface from Fig. 9a due to the large gradient in θ; subtracting the average gradient gives a clearer picture of the underlying structure (Fig. 9b).

As an example of why direct integration cannot be used, time histories for a second hypothetical system are shown in Fig. 10, comparing direct integration and the novel method. For both models $A_u = 20$ and $K = 1$. Limit-cycle amplitude A is initially 5 but is changed discontinuously to zero at $t = 5$ s. The direct integration method fails at this point; however, τ adjusts accordingly and produces the correct decay to a fixed point.

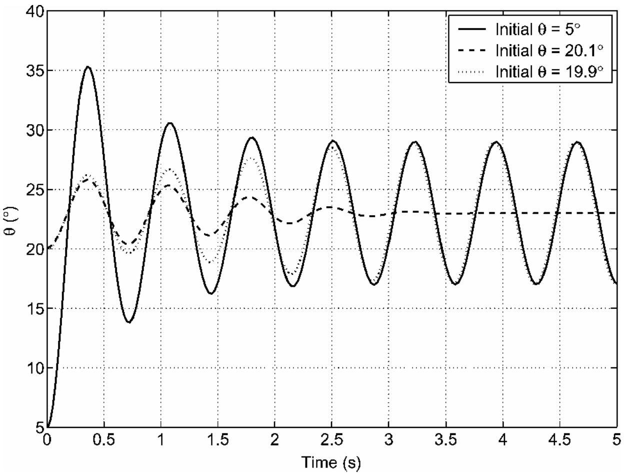

Fig. 8 Time simulations for three initial conditions.

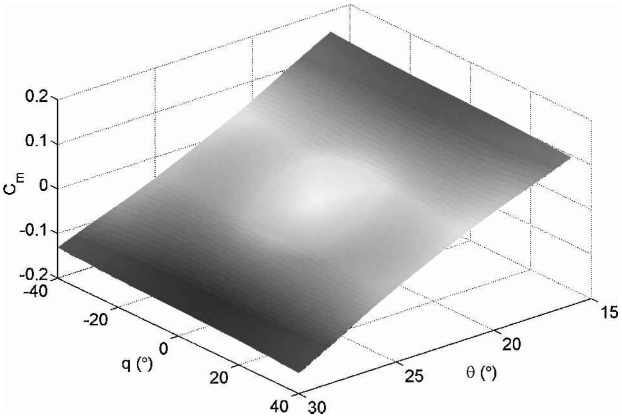

Fig. 9a $C_m(\hat{\theta}, \hat{q})$ surface for $\delta_e = -20$ deg.

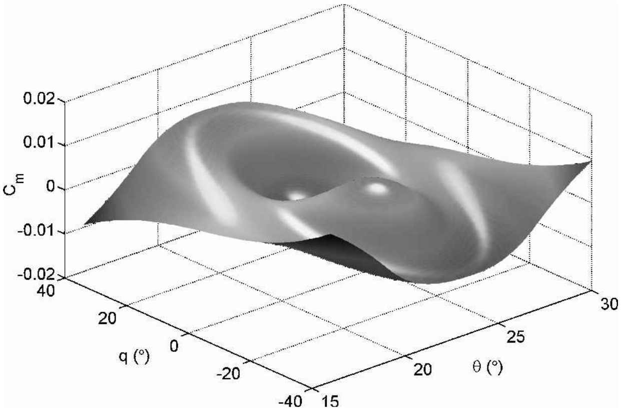

Fig. 9b $C_m(\hat{\theta}, \hat{q})$ surface with the average gradient (in $\hat{\theta}$) removed.

B. Parameter Estimation

The second stage necessary to complete the derivation of a mathematical model of the experimental system is to find values of all of the parameters used in the estimation process. The parameters we need to find can be broadly grouped into two categories: those that relate to the characteristics of the limit-cycle oscillations, A and ω, and those that are related to the shape of the tanh function, K and A_u. The estimated parameter values are listed in Table 1.

Because we are interested in modeling the rig behavior for different values of the tailplane deflection, we need to tabulate these parameters as functions of δ_e. For this purpose, we propose to make explicit use of the experimental bifurcation analysis carried out on the rig and presented in Sec. IV.

Table 1 Model parameters (all angles in degrees)

δ_e	Trim angle	A_1	S_1	A_2	S_2	A_3	S_3	A_4	S_4	ω, rads^{-1}	K
0	5.3	0	U	2	S	$A_{\max}^{a}$	U	——	——	5.8	0.8
_5	12.5	0	S	$A_{\max}$	U	——	——	——	——	6.2	0.5
_10	18.5	0	U	0.9	S	$A_{\max}$	U	——	——	7.7	0.4
_15	20.9	0	U	5.5	S	$A_{\max}$	U	——	——	8.6	1.0
_20	22.8	0	S	3.6	U	6.4	S	$A_{\max}$	U	8.6	1.0
_25	25.6	0	S	$A_{\max}$	U	——	——	——	——	8.6	1.0

[a] This limit cycle is to bound the model. In practice, we choose a value that will encompass all attainable θ.

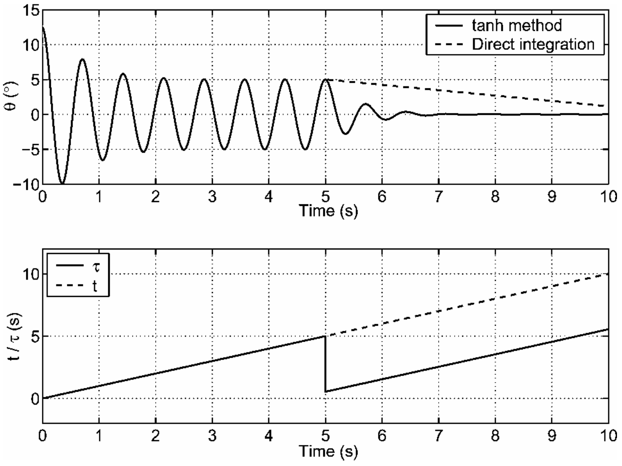

Fig. 10 Comparison of direct integration and novel strategy.

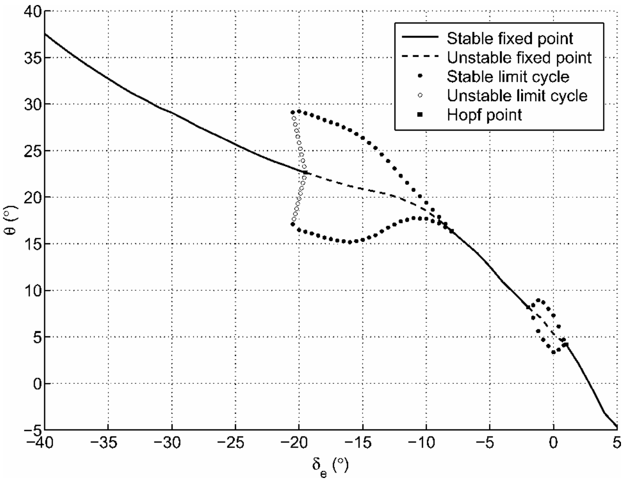

Fig. 11 Desired bifurcation diagram for the system model.

1. Limit-Cycle Amplitude A

From the experimental bifurcation diagram (Fig. 1), it is possible to extract the bifurcation diagram we want the model to exhibit. This is obtained by finding the trim curve (corresponding to the branch of stable and unstable equilibria in the diagram) and by appropriately fitting the limit-cycle amplitudes (found by averaging data readings from Fig. 1). The result of this process is shown in Fig. 11.

Nonlinear dynamics theory dictates that there must be a branch of unstable equilibria inside the limit cycles as these originate from a Hopf bifurcation point, hence, the dashed lines in Fig. 11. These unstable fixed points cannot be found in the experimental system, thus, for the sake of simplicity, they were placed in the center of the limit cycle. (Theoretically they could be found by trial and error by releasing the model from rest near an unstable equilibrium and observing the response, but the level of tunnel turbulence is too high for that to be an option in this case.) In practice, though, the limit cycles are not necessarily symmetrical about the unstable fixed points, as discussed in Sec. VI.

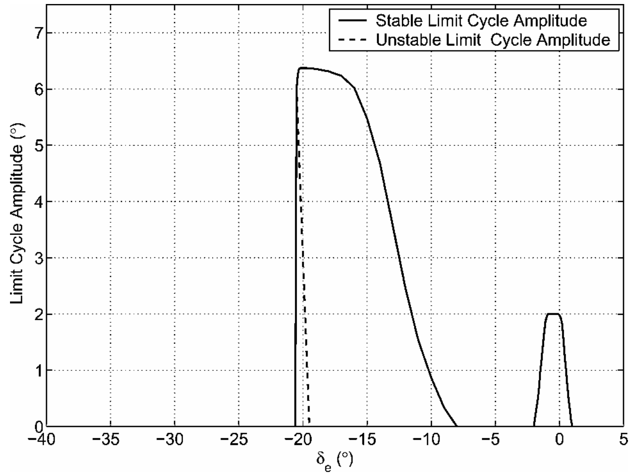

Fig. 12 Trim curve and limit-cycle amplitudes as functions of tailplane deflection.

Once the desired model bifurcation diagram has been obtained, the amplitudes A of the limit cycles as a function of tailplane deflection can be extracted. Figure 12 shows the limit-cycle amplitudes as a function of δ_e (just a different representation of Fig. 11).

Notice that care must be taken when using this interpolated data to ensure that errors are not introduced at discontinuities. For example, when the stable limit cycle disappears at the cyclic fold ($\delta_e \approx$ _21 deg), its corresponding amplitude must go discontinuously to zero because the oscillatory behavior is no longer present. (This causes the jump at $\delta_e \approx$ _20 deg observed in Fig. 12) In the numerical implementation, a simple conditional statement is used to overcome this problem.

2. Growth/Decay Rate and Frequency, K and ω

The growth (decay) rates K and the oscillation frequencies as functions of the tailplane deflection were found by recording experimental time histories at different values of δ_e. By the comparison of experimental results (such as Fig. 6) with time simulations of the model for different values of K and ω, the best fits for these parameters were found by direct investigation.

When this procedure was repeated for several values of the elevator deflections and linear interpolation was used, the parameters K and ω were tabulated over the δ_e range of interest (Table 1). Note that this process could be automated using parameter identification methods, but due to the structure of the model, this would be complicated and was not seen to be necessary at this stage. Fourier transforming the time series could be used to find the frequency of oscillations, but again was not adopted here.

Table 1 shows the tabulated parameters for the model, where A_i represents the amplitude and S_i the stability of the ith limit cycle/fixed point. The number of equilibria varies according to the tailplane deflection; however, there is always a fixed point at the trim angle (amplitude zero, A_1 and S_1), and an unstable limit cycle with amplitude $A_{\max}$ to bound the model. Where there are additional limit cycles, their amplitude and stability must also be specified, for example, A_2 and S_2. Trim angle and limit-cycle amplitudes are tabulated against tailplane deflection every 0.1 deg, but only 5-deg intervals are shown in Table 1.

3. *Parameters A_u and Δ*

The final step is to find appropriate values for the parameters A_u and Δ in Eq. (2). Note that, as shown in Fig. 7b, these parameters are related to the amplitude of the limit cycles to which θ, as defined by Eq. (2), tend as $t \to \infty$ and the amplitude of the asymptotic limit cycles (equal to zero in the case of equilibria) exhibited for $t \to \infty$. In particular, A_u is the amplitude of the limit cycle for $t \to -\infty$ and $A_u - 2\Delta$ that of the limit cycle for $t \to \infty$.

Thus, for the model to match asymptotically the experimental rig, we need to have

$$\Delta = \tfrac{1}{2}(A_u - A) \tag{27}$$

Moreover, to account for whether the envelope is increasing or decreasing, we have to choose A_u at the current time step so that the envelope is increasing if the trajectory, θ_n and $\dot{\theta}_n$, is inside the target asymptotic limit cycle and decreasing otherwise.

Assume, for the sake of simplicity, that the limit cycles of interest are approximately circular. It is easy to show that the relative position of a pair of given initial conditions can be checked by using the following criterion:

$$\frac{\theta^2}{A^2} + \frac{\dot{\theta}^2}{(A\omega)^2} \begin{cases} < 1 & \text{if inside the limit cycle} \\ = 1 & \text{if on the limit cycle} \\ > 1 & \text{if outside the limit cycle} \end{cases}$$

Accordingly, we then set A_u as an arbitrarily large value, $A_u \gg A$, if the current trajectory is outside the limit cycle, whereas we choose a suitable value $0 \leq A_u < A$, if inside. Note that, in the case of a coexisting stable limit cycle and a stable equilibrium [as in the hysteretic region of the bifurcation diagram (Fig. 3)], A_u should be chosen as close as possible to the amplitude of the unstable limit cycle, which, according to a well-established result in nonlinear dynamics, must exist between the two stable solutions.

Repeating this procedure at each step of the estimation process allows the correct evaluation of all of the parameters of interest. We will now validate the estimator constructed according to the model structure and parameter evaluation strategy described for different operating regimes.

VI. Model Validation

A. Bifurcation Diagram and Time Histories

With the system parameters tabulated against tailplane deflection, it is now possible to use a numerical continuation package to find the bifurcation diagram of the numerical model. [AUTO 97 (Ref. 28) was used in this case.]

It was found that, for continuation purposes, it is not essential to have a good fit of the parameter K because the continuation software is only locating equilibria. However, AUTO was extremely sensitive to stepsize (in tailplane deflection, δ_e) along the unstable limit-cycle branch: The minimum stepsize had to be made extremely small, $\approx 1 \times 10^{-9}$ deg, due to the large gradient of this branch.

The bifurcation diagram produced by AUTO is shown in Fig. 13. It can be seen that, as expected, the model bifurcation diagram matches well the experimental one and is actually identical to the desired one shown in Fig. 11.

The time histories in Fig. 14 show good agreement between the experimental results and the numerical model. Note that when the limit-cycle amplitudes are small or zero (as in the case of equilibria), for example, Figs. 14a–14c ($t > 8$s), the effects of low-frequency tunnel turbulence causes some discrepancies between the predicted and experimental results. Turbulence is also found to affect the experimental response when large-amplitude limit-cycle behavior is present, for example, Figs. 14d and 14e ($t > 9$s), causing the experimental results to exhibit a slight phase and amplitude mismatch when compared to simulation results. Nevertheless, when parameters are tabulated against tailplane deflection, the mathematical model adequately represents the experimental system. Note that in some of the experimental time histories the oscillation frequency seems to vary with amplitude. This could be modeled by making frequency ω a function of both tailplane deflection and limit-cycle amplitude. However, there is only a small error caused by this, and therefore, it has been ignored here.

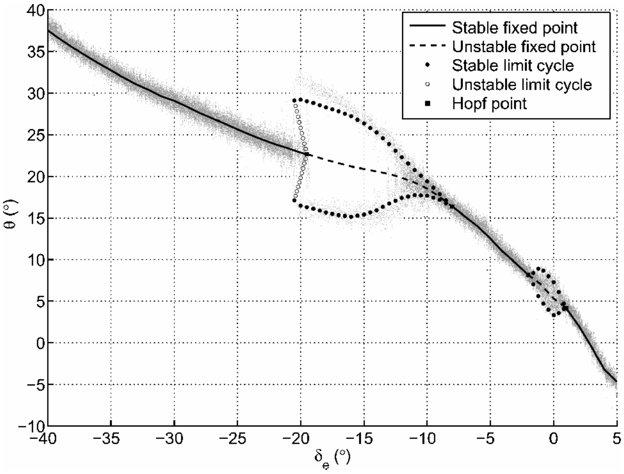

Fig. 13 Bifurcation diagram produced by AUTO 97 numerical continuation package, with experimental results in gray.

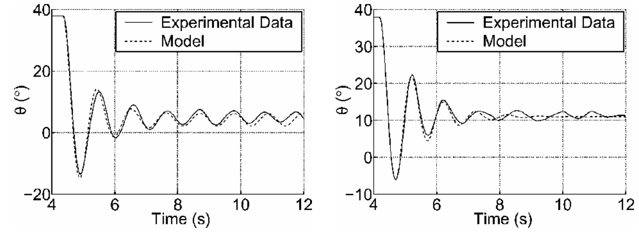

a) $\delta_e = 0$ deg, $k = 0.8$, $\omega = 5.8$ rad/s

b) $\delta_e = -5$ deg, $k = 0.52$, $\omega = 6.2$ rad/s

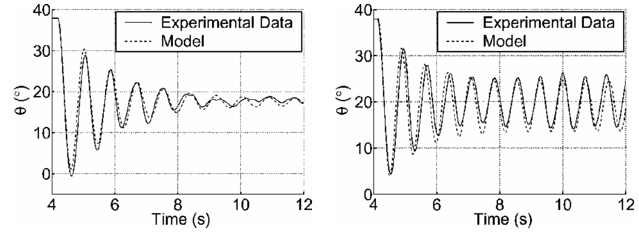

c) $\delta_e = -10$ deg, $k = 0.35$, $\omega = 7.7$ rad/s

d) $\delta_e = -15$ deg, $k = 1$, $\omega = 8.6$ rad/s

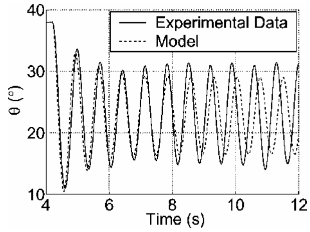

e) $\delta_e = -20$ deg, $k = 1$, $\omega = 8.6$ rad/s

Fig. 14 Comparison of experimental and model time histories at several tailplane deflections; discrepancies between results are due to large, low-frequency tunnel turbulence.

B. Discussion

1. *Limit-Cycle Asymmetry*

A relatively large error (approximately 3 deg at its maximum) can be seen in Fig. 13 between the maximum θ of the large limit cycle ($-20 < \delta_e < -15$ deg) for the experimental system and the model. This is possibly due to the limit cycle being asymmetric but, as already mentioned, it is not possible to find the unstable fixed points in free-oscillation tests and so this cannot be validated. However, the unstable branches could be found from static tests, or by increasing pitch damping via mechanical, for example, an oil-filled damper at the gimbal, or aerodynamic, for example, canards with q feedback, means.

It is also possible for the model to accommodate an asymmetric limit cycle by adding an offset multiplied by a tanh function to Eq. (2). The offset value could then be tabulated against tailplane deflection, giving variable asymmetry and a closer match between model and experimental bifurcation diagrams.

2. *Limit-Cycle Shape*

Often, limit-cycle oscillations cannot be approximated adequately by a pure sine wave. Therefore, it is useful to be able to model limit cycles of arbitrary shape. When the output of several models produced using the technique presented here (with different frequencies and amplitudes) are summed, it is possible in theory to produce any shape of limit cycle. An experimental time history of a limit-cycle oscillation of arbitrary shape can, therefore, be Fourier transformed and the dominant sin/cos components used in the model. In this way it is also possible to model limit cycles with periods greater than 1 and to model the associated period-doubling bifurcations.

3. *Generalization of the Model*

With the model constructed and validated, as described above, it is now possible to proceed with development, testing and comparison of control laws. A particular application of interest is 'bifurcation tailoring'—the use of feedforward and feedback controllers to alter the bifurcation diagram to have desired properties.[29,30] Preliminary results on the use of the model for control system design are presented elsewhere.[31]

For general modeling of non-linear systems it is possible to use the method presented here to model types of bifurcation other than Hopf points. When limit-cycle amplitudes of zero are used, systems with fold and pitchfork bifurcations can be created, where decay onto the stable fixed points is exponential in nature. The problem becomes one of tabulating the data for the bifurcation diagram branches and ensuring that the model is correct when discontinuities in the data are necessary for example, at a fold point. Other types of decay/growth other than exponential are also possible in theory; however, in the majority of cases it is adequate to assume an exponential form.

The type of model presented here, derived from measured motion variables, can in principle be extended to more DOF. For coupled motions, however, the model would become more difficult to visualize because aerodynamic coefficients would be functions of several state variables.

VII. Conclusions

In this paper, experimental results from a single-DOF dynamic wind-tunnel rig were presented. The results show some interesting nonlinear behavior, including limit cycles and Hopf points. The motivation for the work is to develop and compare feedback control systems; to do this, a representative model of the rig is needed. After it was established that traditional aerodynamic modeling methods do not allow multiple-attractor bifurcationary systems to be modeled easily, a new modeling approach was developed. This method requires assumptions regarding limit-cycle orbit shapes and growth/decay functions; in this case, that the limit-cycle oscillations are sinusoidal and that the growth and decay from/to equilibria are exponential in nature. Given experimental time histories, although masked by tunnel turbulence, these assumptions seem valid. With the development of a structure for the model, limit-cycle amplitudes, frequency, and stability are specified as functions of parameters. An analytical solution for the acceleration that gives this motion allows the pitching moment coefficient C_m to be calculated as a function of θ and $\dot{\theta}$.

By use of the novel method presented here, the amount of data storage required is greatly reduced from that of a traditional stability derivative model. In the single-DOF case with one parameter, a two-dimensional table of derivatives can be replaced by five, one-dimensional tables. The advantage of this method increases as more DOF or parameters are added.

Comparison of the experimental and model bifurcation diagrams have shown good agreement. Both supercritical and subcritical Hopf points have been created in the correct location, and limit-cycle amplitudes correspond well. Time simulations have been compared with experimental time histories and also serve to validate the model. The extension and generalization of the model are discussed.

Investigation into the relationship between the flow physics and observed motions is to be carried out using visualization techniques. Future work will also address the issue of using the mathematical model presented here to validate and design appropriate control laws to be implemented and tested on the experimental rig.

Acknowledgments

Funding for the pendulum rig apparatus by QinetiQ Bedford is gratefully acknowledged as is the funding of this work by the Engineering and Physical Sciences Research Council (EPSRC). We would also like to thank Hilton Kyle and Ian Roberts for their input to this paper.

References

[1] Herbst, W. B., "Future Fighter Technologies," *Journal of Aircraft*, Vol. 17, No. 8, 1980, pp. 561–566.

[2] Hanff, E. S., "Direct Forced-Oscillation Techniques for the Determination of Stability Derivatives in Wind Tunnels," *Dynamic Stability Parameters*, AGARD LS-114 March 1981, Chap. 4.

[3] Orlick-Ruckemann, K. J. (ed.), "Report of the Fluid Dynamics Panel Working Group 11—Rotary-Balance Testing for Aircraft Dynamics," Technical Rept. AGARD-AR-265, Dec. 1990.

[4] Beyers, M. E., "New Concept for Aircraft Dynamic Stability Testing," *Journal of Aircraft*, Vol. 20, No. 1, 1983, pp. 5–14.

[5] Lowenberg, M. H., and Kyle, H. L., "Development of a Pendulum Support Rig Dynamic Wind Tunnel Apparatus," AIAA Paper 2002-4879, Aug. 2002.

[6] Strogatz, S. H., *Nonlinear Dynamics and Chaos with Applications to Physics, Biology, Chemistry and Engineering*, Addison-Wesley, Reading, MA, 1994.

[7] Virgin, L. N., *Introduction to Experimental Nonlinear Dynamics*, Cambridge Univ. Press, Cambridge, England, U.K., 2000.

[8] Trickey, S. T., and Virgin, L. N., and Dowell, E. H., "The Stability of Limit Cycle Oscillations in a Nonlinear Aeroelastic System," *Proceedings of the Mathematical, Physical and Engineering Sciences*, Royal Society, Vol. 458, No. 2025, Sept. 2002, pp. 2203–2226.

[9] Liebst, B. S., "The Dynamics, Prediction, and Control of Wing Rock in High-Performance Aircraft," *Philosophical Transactions: Mathematical, Physical and Engineering Sciences*, 356(1745), October 1998.

[10] Hsu, C.-H., and Lan, C. E., "Theory of Wing Rock," *Journal of Aircraft*, Vol. 22, No. 10, 1985, pp. 920–924.

[11] Tobak, M., and Schiff, L. B., "Aerodynamic Mathematical Modelling Basic Concepts," *AGARD Lecture Series on Dynamic Stability Parameters*, AGARD LS-114, NATO, April 1981, Chap. 1.

[12] Goman, M. G., and Khrabrov, A., "State-Space Representation of Aerodynamic Characteristics of an Aircraft at High Angles of Attack," *Journal of Aircraft*, Vol. 31, No. 5, 1994, pp. 1109–1115.

[13] Klein, V., and Noderer, K. D., "Modelling of Aircraft Unsteady Aerodynamic Characteristics. Part 1—Postulated Models," NASA Technical Rept. TM 109120, May 1994.

[14] Myatt, H. J., "A Nonlinear Indicial Response Model for the Rolling 65-Degree Delta Wing," AIAA Paper 96-3406, Aug. 1996.

[15] Ross, A. J., and Nguyen, L. T., "Some Observations Regarding Wing Rock Oscillations at High Angles of Attack," Royal Aerospace Establishment, Technical Rept. RAE TM Aero. 2143, Farnborough, UK, Sept. 1988.

[16] Guglieri, G., and Quagliotti, F., "Experimental Observation and Discussion of the Wing Rock Phenomenon," *Aerospace Science and Technology*, Vol. 1, No. 2, 1997, pp. 111–123.

[17] Vaidya, S. D., and Ananthkrishnan, N., "Adaptive Control of Slender Delta Wing Rock in Stability Wind Tunnel," *Journal of the Aeronautical Society of India*, Vol. 49, No. 4, 1997, pp. 183–187.

[18] Nguyen, L. T., and Yip, L., and Chambers, J. R., "Self-Induced Wing Rock of Slender Delta Wings," AIAA Paper 81-1883, Aug. 1981.

[19] Schmidt, L. V., "Wing Rock Due to Aerodynamic Hysteresis," *Journal of Aircraft*, Vol. 16, No. 3, 1979, pp. 129–133.

[20] Ross, A. J., "Review and Extension of Analysis of Wing Rock Oscillations," Royal Aerospace Establishment, Technical Rept. RAE TR 89051, Farnborough, UK, Oct. 1989.

[21] Ericsson, L. E., Mendenhall, M. R., and Perkins, S. C., “Review of Forebody-Induced Wing Rock,” *Journal of Aircraft*, Vol. 33, No. 2, 1996, pp. 253–259.

[22] Schmidt, L. V., *Introduction to Flight Dynamics*, AIAA Education Series, AIAA Reston, VA, 1998, Chap. 8.

[23] Hui, W. H., and Tobak, M., “Bifurcation Theory Applied to Aircraft Motions,” NASA Technical Rept. TM-86704, March 1985.

[24] Lieven, N., “Solar Heliospherical Observatory—Attitude Control Unit (ACU) Tri-Axis Moment of Inertia Measurements,” Aerospace Engineering Dept. Rept. Ae/bae/ss/01, Univ. of Bristol, Bristol, England, U.K., Aug. 1992.

[25] Orlik-Ruckemann, K. J., “Aerodynamic Aspects of Aircraft Dynamics at High Angles of Attack,” *Journal of Aircraft*, Vol. 20, No. 9, 1983, pp. 737–752.

[26] Hsiao, F. B., and Yang, J. S., “The Study of Wing-Rock Characteristics on Slender Delta Wings at High Angle-of-Attack,” International Council of Aeronautical Sciences, Paper ICAS-96-3.1.1, Sept. 1996.

[27] Hanff, E. S., “Large Amplitude Oscillations,” *Special Course on Aircraft Dynamics at High Angles-of-Attack: Experiments and Modelling*, AGARD R-776 April 1991, Chap. 4.

[28] Doedel, E. J., and Champneys, A. R., and Fairgrieve, T. F., Kuznetsov, Y. A., Sandstede, B., and WANG, X., “AUTO 97: Continuation and Bifurcation Software for Ordinary Differential Equations (with homcont),” Technical Rept., Concordia Univ., Montreal, QC, Canada, March 1998.

[29] Charles, G. A., and Di Bernardo, M., and Lowenberg, M. H., and Stoten, D. P., and Wang, X. F., “Bifurcation Tailoring of Equilibria: A Feedback Control Approach,” *Latin American Applied Research Journal*, Vol. 31, No. 3, 2001, pp. 199–210.

[30] Wang, X. F., Charles, G. A., and Lowenberg, M. H., and Stoten, D. P., and Di Bernardo, M., “Bifurcation Tailoring via Newton Flow Aided Adaptive Control,” *International Journal of Bifurcation and Chaos*, Vol. 13, No. 3, 2003, pp. 677–684.

[31] Davison, P. M., di Bernardo, M., and Lowenberg, M. H., “Modelling and Control of a Single Degree-of-Freedom Dynamic Wind Tunnel Rig,” To be Presented at European Control Conference 2003 (ECC2003), Univ. of Cambridge, UK, Sept. 2003.